

2 In-situ calibration of the single-photoelectron charge 3 response of the IceCube photomultiplier tubes



4 ICECUBE

5 IceCube collaboration

6 M. G. Aartsen,^p M. Ackermann,^{bc} J. Adams,^p J. A. Aguilar,^l M. Ahlers,^t M. Ahrens,^{at}
7 C. Alispach,^z K. Andeen,^{ak} T. Anderson,^{az} I. Ansseau,^l G. Anton,^x C. Argüelles,ⁿ
8 J. Auffenberg,^a S. Axani,ⁿ P. Backes,^a H. Bagherpour,^p X. Bai,^{aq} A. Balagopal V.,^{ac}
9 A. Barbano,^z S. W. Barwick,^{ab} B. Bastian,^{bc} V. Baum,^{aj} S. Baur,^l R. Bay,^h J. J. Beatty,^{r,s}
10 K.-H. Becker,^{bb} J. Becker Tjus,^k S. BenZvi,^{as} D. Berley,^q E. Bernardini,^{bc,bd}
11 D. Z. Besson,^{ad,be} G. Binder,^{h,i} D. Bindig,^{bb} E. Blaufuss,^q S. Blot,^{bc} C. Boehm,^{at} M. Börner,^u
12 S. Böser,^{aj} O. Botner,^{ba} J. Böttcher,^a E. Bourbeau,^t J. Bourbeau,^{ai} F. Bradascio,^{bc}
13 J. Braun,^{ai} S. Bron,^z J. Brostean-Kaiser,^{bc} A. Burgman,^{ba} J. Buscher,^a R. S. Busse,^{al}
14 T. Carver,^z C. Chen,^f E. Cheung,^q D. Chirkin,^{ai} S. Choi,^{av} K. Clark,^{ae} L. Classen,^{al}
15 A. Coleman,^{am} G. H. Collin,ⁿ J. M. Conrad,ⁿ P. Coppin,^m P. Correa,^m D. F. Cowen,^{ay,az}
16 R. Cross,^{as} P. Dave,^f C. De Clercq,^m J. J. DeLaunay,^{az} H. Dembinski,^{am} K. Deoskar,^{at}
17 S. De Ridder,^{aa} P. Desiati,^{ai} K. D. de Vries,^m G. de Wasseige,^m M. de With,^j T. DeYoung,^v
18 A. Diaz,ⁿ J. C. Díaz-Vélez,^{ai} H. Dujmovic,^{av} M. Dunkman,^{az} E. Dvorak,^{aq} B. Eberhardt,^{ai}
19 T. Ehrhardt,^{aj} P. Eller,^{az} R. Engel,^{ac} P. A. Evenson,^{am} S. Fahey,^{ai} A. R. Fazely,^g J. Felde,^q
20 K. Filimonov,^h C. Finley,^{at} D. Fox,^{ay} A. Franckowiak,^{bc} E. Friedman,^q A. Fritz,^{aj}
21 T. K. Gaisser,^{am} J. Gallagher,^{ah} E. Ganster,^a S. Garrappa,^{bc} L. Gerhardt,ⁱ K. Ghorbani,^{ai}
22 T. Glauch,^y T. Glüsenkamp,^x A. Goldschmidt,ⁱ J. G. Gonzalez,^{am} D. Grant,^v Z. Griffith,^{ai}
23 S. Griswold,^{as} M. Günder,^a M. Gündüz,^k C. Haack,^a A. Hallgren,^{ba} L. Halve,^a F. Halzen,^{ai}
24 K. Hanson,^{ai} A. Haungs,^{ac} D. Hebecker,^j D. Heereman,^l P. Heix,^a K. Helbing,^{bb} R. Hellauer,^q
25 F. Henningsen,^y S. Hickford,^{bb} J. Hignight,^w G. C. Hill,^b K. D. Hoffman,^q R. Hoffmann,^{bb}
26 T. Hoinka,^u B. Hokanson-Fasig,^{ai} K. Hoshina,^{ai,be} F. Huang,^{az} M. Huber,^y T. Huber,^{ac,bc}
27 K. Hultqvist,^{at} M. Hünnefeld,^u R. Hussain,^{ai} S. In,^{av} N. Iovine,^l A. Ishihara,^o G. S. Japaridze,^e
28 M. Jeong,^{av} K. Jero,^{ai} B. J. P. Jones,^d F. Jonske,^a R. Joppe,^a D. Kang,^{ac} W. Kang,^{av}
29 A. Kappes,^{al} D. Kappesser,^{aj} T. Karg,^{bc} M. Karl,^y A. Karle,^{ai} U. Katz,^x M. Kauer,^{ai}
30 J. L. Kelley,^{ai} A. Kheirandish,^{ai} J. Kim,^{av} T. Kintscher,^{bc} J. Kiryluk,^{au} T. Kittler,^x
31 S. R. Klein,^{h,i} R. Koirala,^{am} H. Kolanoski,^j L. Köpke,^{aj} C. Kopper,^v S. Kopper,^{ax}
32 D. J. Koskinen,^t M. Kowalski,^{j,bc} K. Krings,^y G. Krücker,^{aj} N. Kulacz,^w N. Kurahashi,^{ap}
33 A. Kyriacou,^b M. Labare,^{aa} J. L. Lanfranchi,^{az} M. J. Larson,^q F. Lauber,^{bb} J. P. Lazar,^{ai}
34 K. Leonard,^{ai} A. Leszczyńska,^{ac} M. Leuermann,^a Q. R. Liu,^{ai} E. Lohfink,^{aj}

35 C. J. Lozano Mariscal,^{al} L. Lu,^o F. Lucarelli,^z J. Lünemann,^m W. Luszczak,^{ai} Y. Lyu,^{h,i}
 36 W. Y. Ma,^{bc} J. Madsen,^{ar} G. Maggi,^m K. B. M. Mahn,^v Y. Makino,^o P. Mallik,^a K. Mallot,^{ai}
 37 S. Mancina,^{ai} I. C. Mariş,^l R. Maruyama,^{an} K. Mase,^o R. Maunu,^q F. McNally,^{ag} K. Meagher,^{ai}
 38 M. Medici,^t A. Medina,^s M. Meier,^u S. Meighen-Berger,^y T. Menne,^u G. Merino,^{ai} T. Meures,^l
 39 J. Micallef,^v D. Mockler,^l G. Momenté,^{aj} T. Montaruli,^z R. W. Moore,^w R. Morse,^{ai} M. Moulai,ⁿ
 40 P. Muth,^a R. Nagai,^o U. Naumann,^{bb} G. Neer,^v H. Niederhausen,^y M. U. Nisa,^v S. C. Nowicki,^v
 41 D. R. Nygren,ⁱ A. Obertacke Pollmann,^{bb} M. Oehler,^{ac} A. Olivas,^q A. O’Murchadha,^l
 42 E. O’Sullivan,^{at} T. Palczewski,^{h,i} H. Pandya,^{am} D. V. Pankova,^{az} N. Park,^{ai} P. Peiffer,^{aj}
 43 C. Pérez de los Heros,^{ba} S. Philippen,^a D. Pieloth,^u E. Pinat,^l A. Pizzuto,^{ai} M. Plum,^{ak}
 44 A. Porcelli,^{aa} P. B. Price,^h G. T. Przybylski,ⁱ C. Raab,^l A. Raissi,^p M. Rameez,^t L. Rauch,^{bc}
 45 K. Rawlins,^c I. C. Rea,^y R. Reimann,^a B. Relethford,^{ap} M. Renschler,^{ac} G. Renzi,^l
 46 E. Resconi,^y W. Rhode,^u M. Richman,^{ap} S. Robertson,ⁱ M. Rongen,^a C. Rott,^{av} T. Ruhe,^u
 47 D. Ryckbosch,^{aa} D. Rysewyk,^v I. Safa,^{ai} S. E. Sanchez Herrera,^v A. Sandrock,^u
 48 J. Sandros,^{aj} M. Santander,^{ax} S. Sarkar,^{ao} S. Sarkar,^w K. Satalecka,^{bc} M. Schaufel,^a
 49 H. Schieler,^{ac} P. Schlunder,^u T. Schmidt,^q A. Schneider,^{ai} J. Schneider,^x
 50 F. G. Schröder,^{ac,am} L. Schumacher,^a S. Sclafani,^{ap} D. Seckel,^{am} S. Seunarine,^{ar}
 51 S. Shefali,^a M. Silva,^{ai} R. Snihur,^{ai} J. Soedingrekso,^u D. Soldin,^{am} M. Song,^q
 52 G. M. Spiczak,^{ar} C. Spiering,^{bc} J. Stachurska,^{bc} M. Stamatikos,^s T. Stanev,^{am} R. Stein,^{bc}
 53 P. Steinmüller,^{ac} J. Stettner,^a A. Steuer,^{aj} T. Stezelberger,ⁱ R. G. Stokstad,ⁱ A. Stöbl,^o
 54 N. L. Strotjohann,^{bc} T. Stürwald,^a T. Stuttard,^t G. W. Sullivan,^q I. Taboada,^f F. Tenholt,^k
 55 S. Ter-Antonyan,^g A. Terliuk,^{bc} S. Tilav,^{am} K. Tollefson,^v L. Tomankova,^k C. Tönnis,^{aw}
 56 S. Toscano,^l D. Tosi,^{ai} A. Trettin,^{bc} M. Tselengidou,^x C. F. Tung,^f A. Turcati,^y R. Turcotte,^{ac}
 57 C. F. Turley,^{az} B. Ty,^{ai} E. Unger,^{ba} M. A. Unland Elorrieta,^{al} M. Usner,^{bc} J. Vandenbroucke,^{ai}
 58 W. Van Driessche,^{aa} D. van Eijk,^{ai} N. van Eijndhoven,^m S. Vanheule,^{aa} J. van Santen,^{bc}
 59 M. Vraeghe,^{aa} C. Walck,^{at} A. Wallace,^b M. Wallraff,^a N. Wandkowsky,^{ai} T. B. Watson,^d
 60 C. Weaver,^w A. Weindl,^{ac} M. J. Weiss,^{az} J. Weldert,^{aj} C. Wendt,^{ai} J. Werthebach,^{ai}
 61 B. J. Whelan,^b N. Whitehorn,^{af} K. Wiebe,^{aj} C. H. Wiebusch,^a L. Wille,^{ai} D. R. Williams,^{ax}
 62 L. Wills,^{ap} M. Wolf,^y J. Wood,^{ai} T. R. Wood,^w K. Woschnagg,^h G. Wrede,^x D. L. Xu,^{ai}
 63 X. W. Xu,^g Y. Xu,^{au} J. P. Yanez,^w G. Yodh,^{ab} S. Yoshida,^o T. Yuan^{ai} and M. Zöcklein^a

64 ^a*III. Physikalisches Institut, RWTH Aachen University, D-52056 Aachen, Germany*

65 ^b*Department of Physics, University of Adelaide, Adelaide, 5005, Australia*

66 ^c*Dept. of Physics and Astronomy, University of Alaska Anchorage, 3211 Providence Dr., Anchorage, AK*
 67 *99508, USA*

68 ^d*Dept. of Physics, University of Texas at Arlington, 502 Yates St., Science Hall Rm 108, Box 19059,*
 69 *Arlington, TX 76019, USA*

70 ^e*CTSPS, Clark-Atlanta University, Atlanta, GA 30314, USA*

71 ^f*School of Physics and Center for Relativistic Astrophysics, Georgia Institute of Technology, Atlanta, GA*
 72 *30332, USA*

73 ^g*Dept. of Physics, Southern University, Baton Rouge, LA 70813, USA*

74 ^h*Dept. of Physics, University of California, Berkeley, CA 94720, USA*

75 ⁱ*Lawrence Berkeley National Laboratory, Berkeley, CA 94720, USA*

76 ^j*Institut für Physik, Humboldt-Universität zu Berlin, D-12489 Berlin, Germany*

77 ^k*Fakultät für Physik & Astronomie, Ruhr-Universität Bochum, D-44780 Bochum, Germany*

78 ^l *Université Libre de Bruxelles, Science Faculty CP230, B-1050 Brussels, Belgium*
79 ^m *Vrije Universiteit Brussel (VUB), Dienst ELEM, B-1050 Brussels, Belgium*
80 ⁿ *Dept. of Physics, Massachusetts Institute of Technology, Cambridge, MA 02139, USA*
81 ^o *Dept. of Physics and Institute for Global Prominent Research, Chiba University, Chiba 263-8522, Japan*
82 ^p *Dept. of Physics and Astronomy, University of Canterbury, Private Bag 4800, Christchurch, New Zealand*
83 ^q *Dept. of Physics, University of Maryland, College Park, MD 20742, USA*
84 ^r *Dept. of Astronomy, Ohio State University, Columbus, OH 43210, USA*
85 ^s *Dept. of Physics and Center for Cosmology and Astro-Particle Physics, Ohio State University, Columbus,*
86 *OH 43210, USA*
87 ^t *Niels Bohr Institute, University of Copenhagen, DK-2100 Copenhagen, Denmark*
88 ^u *Dept. of Physics, TU Dortmund University, D-44221 Dortmund, Germany*
89 ^v *Dept. of Physics and Astronomy, Michigan State University, East Lansing, MI 48824, USA*
90 ^w *Dept. of Physics, University of Alberta, Edmonton, Alberta, Canada T6G 2E1*
91 ^x *Erlangen Centre for Astroparticle Physics, Friedrich-Alexander-Universität Erlangen-Nürnberg, D-91058*
92 *Erlangen, Germany*
93 ^y *Physik-department, Technische Universität München, D-85748 Garching, Germany*
94 ^z *Département de physique nucléaire et corpusculaire, Université de Genève, CH-1211 Genève, Switzerland*
95 ^{aa} *Dept. of Physics and Astronomy, University of Gent, B-9000 Gent, Belgium*
96 ^{ab} *Dept. of Physics and Astronomy, University of California, Irvine, CA 92697, USA*
97 ^{ac} *Karlsruhe Institute of Technology, Institut für Kernphysik, D-76021 Karlsruhe, Germany*
98 ^{ad} *Dept. of Physics and Astronomy, University of Kansas, Lawrence, KS 66045, USA*
99 ^{ae} *SNOLAB, 1039 Regional Road 24, Creighton Mine 9, Lively, ON, Canada P3Y 1N2*
100 ^{af} *Department of Physics and Astronomy, UCLA, Los Angeles, CA 90095, USA*
101 ^{ag} *Department of Physics, Mercer University, Macon, GA 31207-0001, USA*
102 ^{ah} *Dept. of Astronomy, University of Wisconsin, Madison, WI 53706, USA*
103 ^{ai} *Dept. of Physics and Wisconsin IceCube Particle Astrophysics Center, University of Wisconsin, Madison,*
104 *WI 53706, USA*
105 ^{aj} *Institute of Physics, University of Mainz, Staudinger Weg 7, D-55099 Mainz, Germany*
106 ^{ak} *Department of Physics, Marquette University, Milwaukee, WI, 53201, USA*
107 ^{al} *Institut für Kernphysik, Westfälische Wilhelms-Universität Münster, D-48149 Münster, Germany*
108 ^{am} *Bartol Research Institute and Dept. of Physics and Astronomy, University of Delaware, Newark, DE 19716,*
109 *USA*
110 ^{an} *Dept. of Physics, Yale University, New Haven, CT 06520, USA*
111 ^{ao} *Dept. of Physics, University of Oxford, Parks Road, Oxford OX1 3PU, UK*
112 ^{ap} *Dept. of Physics, Drexel University, 3141 Chestnut Street, Philadelphia, PA 19104, USA*
113 ^{aq} *Physics Department, South Dakota School of Mines and Technology, Rapid City, SD 57701, USA*
114 ^{ar} *Dept. of Physics, University of Wisconsin, River Falls, WI 54022, USA*
115 ^{as} *Dept. of Physics and Astronomy, University of Rochester, Rochester, NY 14627, USA*
116 ^{at} *Oskar Klein Centre and Dept. of Physics, Stockholm University, SE-10691 Stockholm, Sweden*
117 ^{au} *Dept. of Physics and Astronomy, Stony Brook University, Stony Brook, NY 11794-3800, USA*
118 ^{av} *Dept. of Physics, Sungkyunkwan University, Suwon 16419, Korea*
119 ^{aw} *Institute of Basic Science, Sungkyunkwan University, Suwon 16419, Korea*
120 ^{ax} *Dept. of Physics and Astronomy, University of Alabama, Tuscaloosa, AL 35487, USA*
121 ^{ay} *Dept. of Astronomy and Astrophysics, Pennsylvania State University, University Park, PA 16802, USA*

122 ^{az}*Dept. of Physics, Pennsylvania State University, University Park, PA 16802, USA*

123 ^{ba}*Dept. of Physics and Astronomy, Uppsala University, Box 516, S-75120 Uppsala, Sweden*

124 ^{bb}*Dept. of Physics, University of Wuppertal, D-42119 Wuppertal, Germany*

125 ^{bc}*DESY, D-15738 Zeuthen, Germany*

126 ^{bd}*also at Università di Padova, I-35131 Padova, Italy*

127 ^{be}*also at National Research Nuclear University, Moscow Engineering Physics Institute (MEPhI), Moscow*
128 *115409, Russia*

129 ^{bf}*Earthquake Research Institute, University of Tokyo, Bunkyo, Tokyo 113-0032, Japan*

130 *E-mail: analysis@icecube.wisc.edu*

131 **ABSTRACT:** We describe an improved in-situ calibration of the single-photoelectron charge distri-
132 **butions** for each of the in-ice Hamamatsu Photonics R7081-02[MOD] photomultiplier tubes in the
133 **IceCube Neutrino Observatory.** The characterization of the individual PMT charge distributions is
134 **important** for PMT calibration, data and Monte Carlo simulation agreement, and understanding the
135 **effect** of hardware differences within the detector. We discuss the single photoelectron identification
136 **procedure** and how we extract the single-photoelectron charge distribution using a deconvolution
137 **of the multiple-photoelectron charge distribution.**

138 **KEYWORDS:** IceCube, single-photoelectron charge distribution, photomultiplier tubes, calibration

139 **ARXIV EPRINT:** [tbd](#)

140 **Contents**

141	1 Introduction	1
142	1.1 Single-photoelectron charge distributions	3
143	1.2 IceCube datasets and software definitions	6
144	2 Extracting the SPE charge templates	7
145	2.1 Single photoelectron pulse selection	7
146	2.2 Characterizing the low-charge region	8
147	2.3 Fitting procedure	9
148	2.4 SPE charge template fit results	10
149	3 Discussion	11
150	3.1 Correlations between fit parameters and DOM hardware differences	11
151	3.2 Fitting parameters variation over time	14
152	3.3 Quantifying observable changes when modifying the PMT charge distributions	14
153	3.3.1 Model comparison	16
154	3.4 SPE charge templates for calibration	16
155	3.5 SPE charge templates in simulation	17
156	4 Conclusion	18

157 **1 Introduction**

158 The IceCube Neutrino Observatory [1, 2] is a cubic-kilometer-sized array of 5,160 photomultiplier
159 tubes (PMTs) buried in the Antarctic ice sheet, designed to observe high-energy neutrinos interacting
160 with the ice [3]. In 2011, the IceCube Collaboration completed the installation of 86 vertical *strings*
161 of PMT modules, eight of which were arranged in a denser configuration known as the DeepCore
162 sub-array [4]. Each string in IceCube contains 60 digital optical modules (DOMs), which contain
163 a single PMT each, as well as all required electronics [5]. The primary 78 strings (excluding
164 DeepCore) are spaced 125 m apart in a hexagonal grid, with the DOMs extending from 1450 m to
165 2450 m below the surface of the ice sheet. The additional DeepCore strings (79-86) are positioned
166 between the centermost strings in the detector, reducing the horizontal DOM-to-DOM distance in
167 this region to between 42 m and 72 m. The lower 50 DOMs on these strings are located in the
168 deepest 350 m of the detector surrounded by the the cleanest ice [6], while the upper ten provide
169 a cosmic ray veto extending down from 1900 m to 2000 m below the surface. Beyond the in-ice
170 detectors, there exists a surface array, IceTop [7], consisting of 81 stations located just above the
171 in-ice IceCube strings. The PMTs located in IceTop operate at a lower gain and the data from these
172 PMTs was not included in the current analysis; however, the IceTop PMTs are calibrated to single
173 photoelectron charge distribution in a similar way as the in-ice PMTs (see Sec. 5.1 in Ref. [7]).

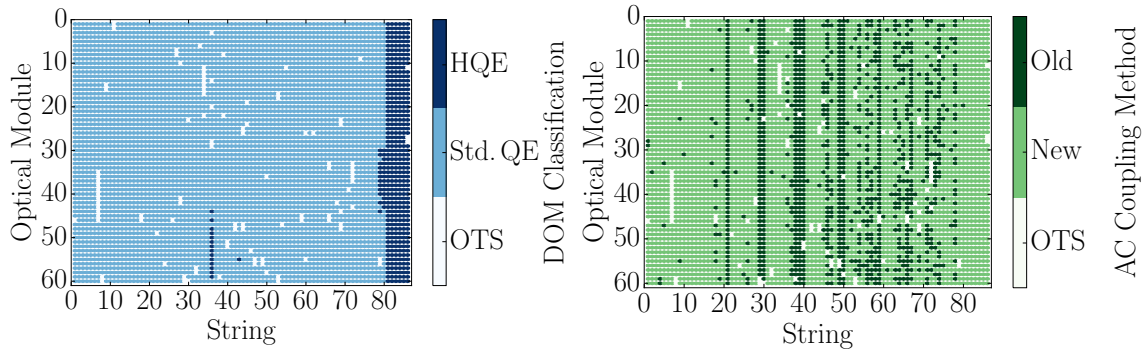


Figure 1. Left: A mapping of the HQE (dark blue) and Standard QE DOMs (light blue). Right: The version of AC coupling, old toroids (dark green) and new toroids (light green). DOMs that have been removed from service (OTS) are shown in white.

174 Each DOM consists of a 0.5"-thick spherical glass pressure vessel that houses a single down-
 175 facing 10" PMT from Hamamatsu Photonics. The PMT is coupled to the glass housing with optical
 176 gel and is surrounded by a wire mesh to reduce the effect of the Earth's ambient magnetic field.
 177 The glass housing is transparent to wavelengths of 350 nm and above [8].

178 Of the 5,160 DOMs, 4,762 house a R7081-02 Hamamatsu Photonics PMT, sensitive to wave-
 179 lengths ranging from 300 nm to 650 nm, with peak quantum efficiency of 25% near 390 nm. These
 180 are classified as Standard Quantum Efficiency (Standard QE) DOMs. The remaining 398 DOMs
 181 are equipped with the Hamamatsu R7081-02MOD PMTs, which, having a peak quantum efficiency
 182 of 34% near 390 nm (36% higher efficiency than the Standard QE DOMs), are classified as High
 183 Quantum Efficiency (HQE) DOMs [4]. These DOMs are primarily located in DeepCore and on
 184 strings 36 and 43, as shown in the left side of Fig. 1.

185 The R7081-02 and R7081-02MOD PMTs have 10 dynode stages and are operated with a
 186 nominal gain of 10^7 and achieved with high voltages ranging from approximately 1215 ± 83 V and
 187 1309 ± 72 V, respectively. A typical amplified single photoelectron generates a 5.2 ± 0.3 mV peak
 188 voltage after digitization with a full width half maximum of 13 ± 1 ns. The PMTs operate with the
 189 anodes at high voltage, so the signal is AC coupled to the amplifiers (front-end amplifiers). There
 190 are two versions of AC coupling in the detectors, referred to as the *new* and *old toroids*, both of
 191 which use custom-designed wideband bifilar wound 1:1 toroidal transformers¹. The locations of
 192 DOMs with the different versions of AC-coupling are shown on the right side of Fig. 1. The DOMs
 193 with the old toroids were designed with an impedance of 43Ω , while the new toroids are 50Ω [9].
 194 All HQE DOMs are instrumented with the new toroids.

195 IceCube relies on two observables per DOM to reconstruct events: the total number of detected
 196 photons and their timing distribution. Both the timing and the number of photons are extracted
 197 from the digitized waveforms. This is accomplished by deconvolving the digitized waveforms [10]
 198 into a series of scaled single photoelectron pulses (so-called pulse series), and the integral of

¹The toroidal transformer effectively acts as a high-pass filter with good signal fidelity at high frequencies and offers a higher level of reliability than capacitive coupling. Conventional AC-coupling high-voltage ceramic capacitors can also produce undesirable noise from leakage currents and are impractical given the signal droop and undershoot requirements [8].

199 the individual pulses divided by the load resistance defines the observed charge. It will often be
200 expressed in units of PE, or photoelectrons, which further divides the measured charge by the charge
201 of a single electron times the nominal gain.

202 When one or more photoelectrons produce a voltage at the anode sufficient to trigger the
203 onboard discriminator, the signal acquisition process is triggered. The discriminator threshold is
204 set to approximately 1.2 mV, or equivalently to ~ 0.23 PE, via a digital-to-analog converter (DAC).
205 The signal is presented to four parallel channels for digitization. Three channels pass through a 75 ns
206 delay loop in order to capture the waveform leading up to the rising edge of the triggering pulse, and
207 are then subject to different levels of amplification prior to being digitized at 300 million samples
208 per second (MSPS) for 128 samples using a 10-bit Analog Transient Waveform Digitizer (ATWD).
209 The high-gain channel has a nominal amplification of 16 and is most suitable for single photon
210 detection. Two ATWD chips are present on the DOM Mainboard (MB) and alternate digitization
211 between waveforms to remove dead time associated with the readout. The signal to the fourth
212 parallel channel is first shaped and amplified, then fed into a 10-bit fast analog-to-digital converter
213 (fADC) operating at a sampling rate of 40 MSPS. Further detail regarding the description of the
214 DOM electronics can be found in Refs. [5, 11].

215 This article discusses a method for determining the in-situ individual PMT single-photoelectron
216 charge distributions, which can be used to improve calibration and the overall detector description
217 in Monte Carlo (MC) simulation. The SPE charge distribution refers to the charge probability
218 density function of an individual PMT generated by the amplification of a pure sample of single
219 photoelectrons. The measured shape of the SPE charge distributions is shown to be useful for
220 examining hardware differences and assessing long term stability of the detector. This was recently
221 made possible with the development of two pieces of software:

- 222 1. A specially-designed unbiased pulse selection developed to reduce the multiple photoelec-
223 tron (MPE) contamination while accounting for other physical phenomena (e.g. late pulses,
224 afterpulses, pre-pulses, and baseline shifts) and software-related effects (e.g. pulse splitting).
225 This is further described in Sec. 2.1.
- 226 2. A fitting procedure developed to separate the remaining MPE contamination from the SPE
227 charge distribution by deconvolving the measured charged distribution. This is further de-
228 scribed in Sec. 2.3.

229 By using in-situ data to determine the SPE charge distributions, we accurately represent the
230 individual PMT response as a function of time, environmental conditions, software version and
231 hardware differences, and realistic photocathode illumination conditions. This is beneficial since
232 it also allows us to inspect the stability and long-term behavior of the individual DOMs, verify
233 previous calibration, and correlate features with specific DOM hardware.

234 1.1 Single-photoelectron charge distributions

235 Ideally, a single photon produces a single photoelectron, which is then amplified by a known
236 amount, and the measured charge corresponds to 1 PE. However, there are many physical processes
237 that create structure in the measured charge distributions. For example:

- 238 • **Statistical fluctuation due to cascade multiplication** [12]. At every stage of dynode
239 amplification, the number of emitted electrons that make it to the next dynode is randomly
240 distributed. This in turn causes a smearing in the measured charge after the gain stage of the
241 PMT.

- 242 • **Photoelectron trajectory**. Some electrons may deviate from the favorable trajectory, re-
243 ducing the number of secondaries produced at a dynode or the efficiency to collect them
244 on the following dynode. This can occur at any stage, but it has the largest effect on the
245 multiplication at the first dynode [13]. The trajectory of a photoelectron striking the first
246 dynode will depend on many things, including where on the photocathode it was emitted,
247 the uniformity of the electric field, the size and shape of the dynodes [12], and the ambient
248 magnetic field [14, 15].

- 249 • **Late or delayed pulses**. A photoelectron can elastically or inelastically backscatter off the first
250 dynode. The scattered electron can then be re-accelerated to the dynode, creating a second
251 pulse. The difference in time between the initial pulse and the re-accelerated pulse in the
252 R7081-02 PMT was previously measured to be up to 70 ns [8, 16]. Elastically backscattered
253 photoelectrons will carry the full energy and are thus expected to produce similar charge to a
254 non-backscattered photoelectron, albeit with a time offset. The mean measured charge of an
255 inelastic backscattered photoelectron, by contrast, is expected to be smaller than a nominal
256 photoelectron [17].

- 257 • **Afterpulses**. When photoelectrons or the secondary electrons produced during the electron
258 cascade gain sufficient energy to ionize residual gas in the PMT, the resulting positively
259 charged ionized gas will be accelerated in the electric field towards the photocathode. Upon
260 impact with the photocathode, electrons can be released from the photocathode, creating
261 what is called an afterpulse. For the R7081-02 PMTs used in IceCube, the timescale for
262 afterpulses was measured to occur from 0.3 to 11 μ s after the initial pulse, with the first
263 prominent afterpulse peak occurring at approximately 600 ns [8]. The spread in the afterpulse
264 time depends on the position of photocathode, the charge-to-mass ratio of the ion produced,
265 and the electric potential distribution [18], whereas the size of the afterpulse is related to the
266 momentum and species of the ionized gas and composition of the photocathode [19].

- 267 • **Pre-pulses**. If an incident photon passes through the photocathode without interaction and
268 strikes one of the dynodes, it can eject an electron that is only amplified by the subsequent
269 stages, resulting in a lower measured charge (lower by a factor of approximately 10). For the
270 IceCube PMTs, the prepulses have been found to arrive approximately 30 ns before the signal
271 from other photoelectrons from the photocathode [8].

- 272 • **MPE contamination**. When multiple photoelectrons arrive at the first dynodes within few
273 nanoseconds of each other, they can be reconstructed by the software as a single MPE pulse.

- 274 • **Dark noise**. Photoelectron emission, not initiated from an external event, can be attributed to
275 thermionic emission from the low work function photocathode and the dynodes, Cherenkov
276 radiations initiated from radioactive decay within the DOM, and field emission from the

277 electrodes. Dark noise originating from thermionic emission from the dynodes is shown in
 278 Ref. [20] to populate the low-charge region.

279 • **Electronic noise.** This refers to the combined fluctuations caused by noise generated from the
 280 analog-frontend and the analog-to-digital converters (ATWDs and fADC). When integrated
 281 over a time window the resulting charge is generally small and centered around zero, thus
 282 only leading to a small broadening in the low charge region. The standard deviation of the
 283 electronic noise was found to be approximately ± 0.11 mV.

284 Beyond the physical phenomena above that modify the measured charge distribution, there is
 285 also a lower limit on the smallest charge that can be extracted. For IceCube, the discriminator only
 286 triggers for peak voltages above the threshold and subsequent pulses in the readout window are
 287 subject to a threshold defined in the software. This software threshold was set conservatively to
 288 avoid extracting pulses that originated from electronic noise. It can be modified to gain access to
 289 lower charge pulses and will be discussed in Sec. 2.2.

290 The standard SPE charge distribution used for all DOMs in IceCube, known as the TA0003
 291 distribution [8], models the above effects as the sum of an exponential plus a Gaussian. The TA0003
 292 distribution represents the average SPE charge distribution extracted from a lab measurement of
 293 118 Hamamatsu R7081-02 PMTs. The measurement was performed in a -32°C freezer using a
 294 pulsed UV LED centered along the axis of the PMT, directly in front of the photocathode.

295 Recently, IceCube has made several lab measurements of the SPE charge distribution of
 296 R7081-02 PMTs using single photons generated from a synchronized short duration laser pulses.
 297 The coincident charge distribution generated by the laser pulses was found to include a steeply
 298 falling low-charge component in the region below the discriminator threshold. To account for this,
 299 a new functional form including a second exponential was introduced. This form of the normalized
 300 charge probability distribution $f(q)_{\text{SPE}} = \text{Exp}_1 + \text{Exp}_2 + \text{Gaussian}$, is referred to as the *SPE charge*
 301 *template* in this article. Explicitly, it is:

$$f(q)_{\text{SPE}} = \frac{P_{e1}}{w_1} \cdot e^{-q/w_1} + \frac{P_{e2}}{w_2} \cdot e^{-q/w_2} + \frac{1 - P_{e1} - P_{e2}}{\sigma \sqrt{\pi/2} \cdot \text{Erfc}[-\mu/(\sigma\sqrt{2})]} \cdot e^{-\frac{(q-\mu)^2}{2\sigma^2}}, \quad (1.1)$$

302 where q represents the measured charge; w_1 and w_2 are the exponential decay widths; and μ , σ are
 303 the Gaussian mean and width, respectively; and we define the normalization coefficients for each of
 304 the components to be: $E_1 = P_{e1}/w_1$, $E_2 = P_{e2}/w_2$, and $N = 1 - P_{e1} - P_{e2}/\sigma\sqrt{\pi/2}\text{Erfc}[-\mu/(\sigma\sqrt{2})]$.
 305 Here, Erfc represents the complementary error function. Eq. 1.1 is the assumed functional shape
 306 of the SPE charge distributions, and the components of Eq. 1.1 are determined in this article for all
 307 in-ice DOMs. IceCube has chosen to define 1 PE as the location of the Gaussian mean (μ) and
 308 calibrates the gain of the individual PMTs prior to the start of each season to meet this definition.
 309 Any overall bias in the total observed charge can be absorbed into an efficiency term, such as the
 310 quantum efficiency. This is valid since the linearity between the total charge collected and the
 311 number of incident photons is satisfied up to ~ 2 V [9], or approximately 375 PE. That is, the average
 312 charge collected from N photons is N times the average charge of the SPE charge distribution, and
 313 the average charge of the SPE charge distribution is always a set fraction of the Gaussian mean.

314 1.2 IceCube datasets and software definitions

315 The amount of observed light depends on the local properties of the ice [6]. Short term climate
316 variations from volcanoes and longer-term variations from atmospheric dust affect the optical
317 properties of the ice, producing nearly horizontal layers. This layered structure affects how much
318 light the DOMs observe, and, with it, the trigger rate. The largest contribution to the IceCube
319 trigger rate comes from downward-going muons produced in cosmic ray-induced showers [21].
320 Cosmic ray muons stopping in the detector cause the individual trigger rates to decrease at lower
321 depths.

322 If a DOM and its nearest or next-to-nearest neighbor observe a discriminator threshold crossing
323 within a set time window, a *Hard Local Coincidence* (HLC) is initiated, and the corresponding
324 waveforms are sampled and read out on the three ATWD channels. Thermionic emission induced
325 dark noise can be present in the readout, however it is suppressed at lower temperatures and is
326 unlikely to trigger an HLC event.

327 After waveform digitization, there is a correction applied to remove measured baseline offsets.
328 Distortions to the waveform, such as from droop and undershoot [8] introduced by the toroidal
329 transformer AC coupling are compensated for in software during waveform calibration by adding
330 the expected reaction voltage of the distortion to the calibrated waveform. If the undershoot
331 voltage drops below 0 ADC counts, the ADC values are zeroed and then compensated for once
332 the waveform is above the minimum ADC input. For each version of the AC coupling, scaled
333 single photoelectron pulse shapes are then fit to the digitized waveforms using software referred to
334 as "WaveDeform" (waveform unfolding process), which determines the individual pulse time and
335 charges and populates a pulse series.

336 The pulse series used in this analysis come from two datasets:

337 1. The **MinBias dataset**. This dataset preserves the full waveform readout of randomly-triggered
338 HLC events, collecting on average 1:1000 events. The largest contribution to this dataset
339 comes from downward-going muons produced in cosmic-ray-induced showers. The average
340 event for this sample is approximately 26 PE distributed over an average of 16 triggered
341 DOMs. The full waveform of these events allows us to extract the raw information about
342 the individual pulses. This dataset will be used to measure the individual PMT charge
343 distributions.

344 2. The **BeaconLaunch dataset**. This dataset is populated with digitized waveforms that are ini-
345 tiated by the electronics (forced-triggered) of a channel that has not gone above the threshold.
346 The forced triggered waveforms are typically used to monitor the individual DOM baselines
347 and thus includes the full ATWD waveform readout. Since this dataset is forced-triggered, the
348 majority of these waveforms represent electronic noise with minimal contamination from ran-
349 dom accidental coincidence SPEs. This dataset will be used to examine the noise contribution
350 to the charge distributions.

351 When using this dataset, the weight of every pulse is multiplied by a factor of 28.4 to account
352 for the livetime difference between the MinBias dataset and the BeaconLaunch dataset.
353 Weight, in this context, refers to the number of photons in the MinBias dataset proportional

354 to one statistical photon in the BeaconLaunch dataset for which both datasets have the same
 355 equivalent livetime.

356 This analysis uses the full MinBias and BeaconLaunch datasets from IceCube seasons 2011 to
 357 2016 [22], subsequently referred to as IC86.2011 to IC86.2016. Seasons in IceCube typically start
 358 in May of the labeled year and end approximately one year later. Calibration is performed before
 359 the start of each season.

360 2 Extracting the SPE charge templates

361 2.1 Single photoelectron pulse selection

362 The pulse selection is the method used to extract candidate, unbiased, single photoelectron pulses
 363 from high-gain ATWD channel while minimizing the MPE contamination. The design of the pulse
 364 selection was such that it avoids collecting afterpulses, does not include late pulses from the trigger,
 365 accounts for the discriminator threshold, reduces the effect of signal droop and undershoot, and
 366 gives sufficient statistics to perform a season-to-season measurement. An illustrative diagram of the
 367 pulse selection is shown in the left side of Fig. 2, while a description of the procedure is detailed
 368 below.

369 We restrict the pulse selection to only extract information from waveforms in which the trigger
 370 pulse does not exceed 10 mV (~ 2 PE) and no subsequent part of the waveform exceeds 20 mV

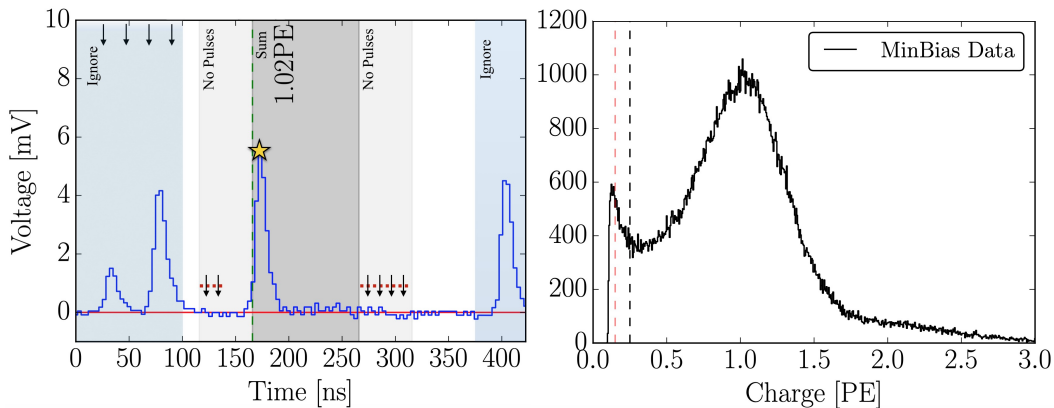


Figure 2. Left: An illustrative diagram of the pulse selection criteria for selecting a high-purity and unbiased sample of single photoelectrons. An example digitized ATWD waveform of data is shown in blue and the baseline is shown as a solid red line. The pulse of interest is identified with a yellow star. This example waveform was triggered by a small pulse at 25 ns (recall that the delay board allows us to examine the waveform just prior to the trigger pulse), followed by a potential late pulse at 70 ns. At 400 ns, we see a pulse in the region susceptible to afterpulses. Waveform voltage checks are illustrated with arrows, and various time windows described in the text are drawn with semi-opaque regions. The POI is reported to have a charge of 1.02 PE, given by WaveDeform, and would pass the pulse selection criteria. Right: The collected charge distribution from string 1, optical module 1 (DOM 1,1), from the MinBias dataset collected from IC86.2011 to IC86.2016 that pass the pulse selection. For visual purposes, the red dashed line and black dotted line indicate 0.15 PE and 0.25 PE respectively. From this, one can see that the pulse selection access charges below the discriminator threshold of 0.23 PE. The fall off in charge around 0.13 PE is due to the software defined threshold from WaveDeform.

371 (~ 4 PE). This reduces the effect of the baseline undershoot due to the AC coupling or other artifacts
372 from large pulses.

373 In order to trigger a DOM, the input to the front-end amplifiers must exceed the discriminator
374 threshold. To avoid the selection bias of the discriminator trigger (i.e. only selecting pulses greater
375 than the discriminator threshold), we ignore the trigger pulse as well as the entire first 100 ns of the
376 time window. Ignoring the first 100 ns removes late pulses that could be attributed to the triggering
377 pulse, which occurs approximately 4% of the time [8]. To ensure we are not accepting afterpulses
378 into the selection, we also enforce the constraint that the pulse of interest (POI) is within the first
379 375 ns of the ATWD time window. This also allows us to examine the waveform up to 50 ns after
380 the POI. In the vicinity of the POI, we ensure that WaveDeform did not reconstruct any pulses up
381 to 50 ns prior to the POI, or 100 to 150 ns after the POI (the light gray region of Fig. 2 (left)). This
382 latter constraint is to reduce the probability of accidentally splitting a late pulse in the summation
383 window.

384 If a pulse is reconstructed between 100 and 375 ns after the start of the waveform and the voltage
385 criteria are met, it is accepted as a candidate photoelectron and several checks are performed on
386 the waveform prior to and after the pulse. The first check is to ensure that the waveform is near the
387 baseline just before the rising edge of the POI. This is accomplished by ensuring that the waveform
388 does not exceed 1 mV, 50 to 20 ns prior to the POI, and eliminates cases where the POI is a late
389 pulse. We also ensure the waveform returns to the baseline by checking that no ADC measurement
390 exceeds 1 mV, 100 to 150 ns after the POI. These constraints are illustrated as the horizontal red
391 dotted lines and black arrows in the left side of Fig. 2.

392 If all the above criteria are met, we sum the reconstructed charges from the POI time, given by
393 WaveDeform, to +100 ns (the dark gray area in Fig. 2 (left)). This ensures that any nearby pulses are
394 either fully separated or fully added. This is important since WaveDeform may occasionally split
395 an SPE pulse into multiple smaller pulses, therefore it is always critical to perform a summation of
396 the charge within a time window. The 100 ns summation also means that the pulse selection will
397 occasionally accept MPE events. We chose 100 ns window for the summation to ensure that we
398 collect the charge of the late pulse (recall that late pulses were measured up to 70 ns after the main
399 pulse), should it be there, while minimizing the MPE contamination. We estimate that there is on
400 average a 6.5% probability of the summation time window includes a MPE pulse.

401 **2.2 Characterizing the low-charge region**

402 This analysis aims to describe the full SPE charge distribution for each DOM. This is required by
403 the IceCube simulation. However, we cannot extract charge to arbitrary low PE before electronic
404 noise starts dominating. The aim of this section is to describe how we extract information in the
405 low-charge region (below 0.25 PE) to guide the full fit. Fig. 2 (right) shows the charge distributions
406 of the selected pulses that pass the single photoelectron pulse selection for string 1, optical module
407 1, DOM(1,1). In the low-charge region, we see a second threshold at approximately 0.13 PE, i.e. the
408 charge distribution terminates. This threshold arises from a termination condition in WaveDeform,
409 in which the pulses that are smaller than predefined criteria are rejected. The threshold was set to
410 avoid electronic noise being interpreted as PMT pulses and contaminating the low-charge region.

411 The steeply falling component of the region from 0.13 PE to 0.25 PE is in agreement with
412 the laser measurements mentioned in Sec. 1.1 and emphasizes the importance of collecting data

413 below the discriminator threshold. This section will assess the noise contribution to this region and
 414 examine the effect on the charge distribution and noise contribution by lowering the WaveDeform
 415 threshold.

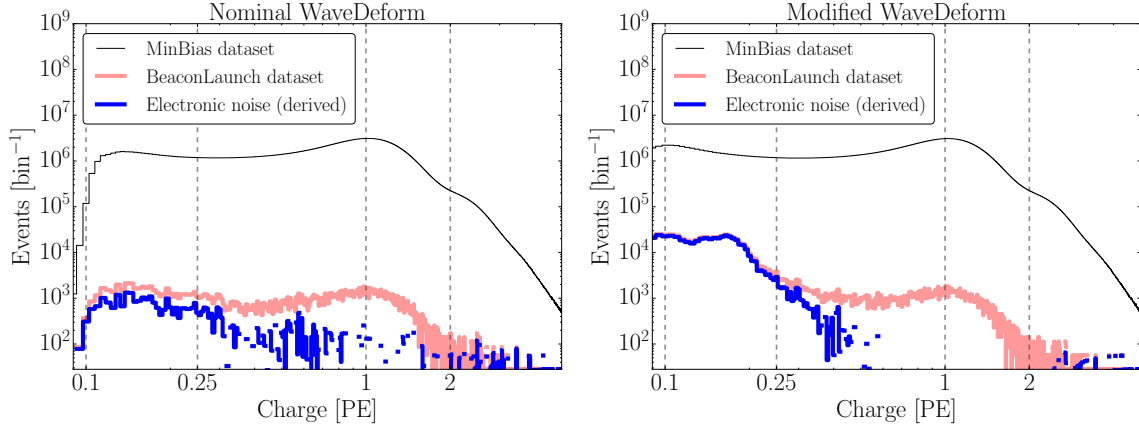


Figure 3. The cumulative charge distributions of all DOMs for the MinBias (M) and BeaconLaunch (B) datasets. The blue histogram shows the derived contribution from electronic noise. This was found by subtracting the normalized MinBias dataset from the BeaconLaunch dataset ($B - M \times (B|_{1PE}/M|_{1PE})$). Left: The charge distributions for the standard WaveDeform settings. Right: The charge distributions for the modified WaveDeform settings.

416 Fig. 3 (left) shows the charge distributions for the MinBias (black) and the BeaconLaunch
 417 (red) datasets using the default settings of WaveDeform (standard WaveDeform). As mentioned
 418 in Sec. 1.2, occasionally a photoelectron will be coincident with the forced BeaconLaunch time
 419 window. These charges populate a SPE charge distribution. Subtracting the shape of the MinBias
 420 charge distribution from the BeaconLaunch dataset yields an estimate of the amount of electronic
 421 noise contamination (blue). The bin in the MinBias data with the lowest signal-to-noise ratio (SNR)
 422 above 0.1 PE was found to have a SNR of 744.7. The SNR for the full distribution was found to be
 423 1.98×10^5 . Fig. 3 (right) shows the same data after lowering the WaveDeform threshold (modified
 424 WaveDeform), and is found to have SNR of 57.9 in the bin with the largest contamination and the
 425 total SNR was found to be 0.69×10^5 .

426 The modified WaveDeform datasets show a minimal increase in the contribution of noise to
 427 the low-charge region. From this, however, we are able to extract charge information down to
 428 approximately 0.10 PE and improve the overall description of the charge distribution below the
 429 discriminator. This will help constrain the values of the steeply falling exponential, defined with
 430 Exp_1 .

431 2.3 Fitting procedure

432 We would now like to fit to the charge distribution to extract the SPE charge templates (the
 433 components of Eq. 1.1) for all DOMs.

434 Contamination from two-photon events is suppressed by the pulse selection, but can not be
435 entirely avoided. To minimize potential biases by the charge entries resulting from two photons,
436 the one and two photon contribution to the charge distributions is fitted at the same time, using
437 something we call a convolutional fitter. It assumes that the charge distribution resulting from two
438 photons is the SPE charge distribution convolved with itself [23]. In each step of the minimizer the
439 convolution is updated given the current set of SPE parameters to be evaluated and the relative one
440 and two photon contributions is determined.

441 We do not account for the three-photon contribution, which is justified by the lack of statistics
442 in the 3 PE region as well as the significant rate difference between the 1 PE and 2 PE region, as
443 shown in Fig. 2 (right).

444 Pulses that fall below the WaveDeform threshold and are not reconstructed contribute to an
445 inefficiency in the individual DOMs. That is, the shape below the WaveDeform software threshold
446 does not have a significant impact, but the relative area of the SPE charge template below compared
447 to above this threshold changes the efficiency of the DOM. This analysis assumes the same shape
448 of the steeply falling exponential component (Exp_1) for all DOMs in the detector to avoid large
449 fluctuations in the DOM-to-DOM efficiencies. The modified WaveDeform data will strictly be
450 used to determine the Exp_1 component. Specifically, using the aggregate of the entire ensemble
451 of DOMs with the modified WaveDeform dataset, we background-subtract the BeaconLaunch
452 distribution from the MinBias data, fit the resulting distribution to determine the components of
453 Eq. 1.1, and use only the measured shape and normalization of Exp_1 in all subsequent standard
454 WaveDeform fits.

455 As described in Sec. 1.1, the Gaussian mean (μ) is used to determine the gain setting for each
456 PMT. Therefore, it is particularly important that the fit quality in this region accurately describes the
457 data. While fitting to the full charge distribution improves the overall fit agreement, the mismatch
458 between the chosen functional form (Eq. 1.1) and a true SPE charge distribution can cause the
459 Gaussian component to pull away from its ideal location. To compensate for this, the fitting
460 algorithm prioritizes fitting to the data around the Gaussian mean. This is accomplished by first
461 fitting to the full distribution to get an estimate of the Gaussian mean location. Then, the data in
462 a the region ± 0.15 PE around the original estimated Gaussian mean is weighted to have a higher
463 impact on the fit, and the distribution is re-fitted.

464 Upon fitting the MinBias dataset with the predetermined values for Exp_1 , the residual of each
465 fit is calculated by measuring the percentage difference between the fit and the data. The average
466 residual is then used as a global scaling factor for all SPE charge templates to account for the
467 difference between the chosen model (Eq. 1.1) and the actual data.

468 2.4 SPE charge template fit results

469 We now present the results of the fits then subsequently describe the correlations of the fit parameters
470 with hardware differences, and time variations in the next section. Using the background-subtracted
471 modified WaveDeform dataset, the Exp_1 component was determined by fitting the aggregate distri-
472 bution from 0.1 PE to 3.5 PE. The result of the fit yielded $E_1 = 6.9 \pm 1.5$ and $w_1 = 0.027 \pm 0.002$ PE.
473 The shape of Exp_1 is now used to describe the low-PE charge region for all subsequent standard
474 WaveDeform fits.

475 Using the MinBias dataset with the measured val-
 476 ues of Exp_1 , the SPE charge templates are extracted for
 477 every DOM, separately for each IceCube season from
 478 IC86.2011 to IC86.2016. The fit range for Exp_2 and the
 479 Gaussian components is selected to be between 0.15 PE
 480 and 3.5 PE. An average fit was also performed on the cu-
 481 mulative charge distribution, in which all the data for a
 482 given DOM was summed together (labeled as "AVG").

483 All the DOMs with "failed fits" are not included in
 484 this analysis. A DOM is classified as having a failed
 485 fit if it does not pass one of the validity checks on the
 486 data requirements (e.g. the number of valid pulses) or
 487 goodness of fit. Between 107 and 111 DOMs over the
 488 seasons considered have been removed from service and
 489 represent the majority of the failed fits. The remaining
 490 6 DOMs that failed the AVG fits are known to have various
 491 issues. In the IceCube MC simulation chain, these DOMs are assigned the average SPE charge
 492 template.

493 We can divide the DOMs into subset of hardware differences: the HQE DOMs with the new
 494 toroids, the Standard QE DOMs with the new toroids, and the Standard QE DOMs with the old
 495 toroids. The mean value and standard error of the IC86.AVG fit parameters, excluding Exp_1 , for the
 496 subset of hardware differences are listed in Table 1. The residual, averaged over all DOMs, from 0
 497 to 1 PE is shown in Fig. 4.

Hardware Configuration	Exp_2 Amp. (E_2)	Exp_2 Width (w_2)	Gaus. Amp. (N)	Gaus. Mean (μ)	Gaus. Width (σ)
HQE / New Toroid	0.261 ± 0.001	0.405 ± 0.003	0.557 ± 0.001	1.0202 ± 0.0010	0.311 ± 0.001
Std. QE / New Toroids	0.228 ± 0.001	0.403 ± 0.001	0.595 ± 0.001	1.0238 ± 0.0004	0.316 ± 0.001
Std. QE / Old Toroids	0.221 ± 0.001	0.420 ± 0.002	0.599 ± 0.001	1.0074 ± 0.0007	0.294 ± 0.001

Table 1. The average values and standard error of each fit parameter for the subset of hardware configurations listed in the first column.

498 An example fit is shown in Fig. 5 for the cumulative MinBias charge distribution for DOM
 499 (1,1). The collected charge distribution is shown in the black histogram, while the fit to the data is
 500 shown as the red line. The extracted SPE charge template from the fit is shown in blue. Both the fit
 501 and extracted SPE charge template have been scaled by the average residual shown in Fig. 4.

502 3 Discussion

503 3.1 Correlations between fit parameters and DOM hardware differences

504 It is evident from the data in Table 1 that the average shape of the SPE charge templates is correlated
 505 with the DOM hardware. These differences can also be seen in the measured peak-to-valley ratios
 506 and average charge of the SPE charge template (see Fig. 6). When we examine the subset of DOMs
 507 instrumented with the new toroids, the average HQE DOM were found to have a $13.8 \pm 0.6\%$ larger

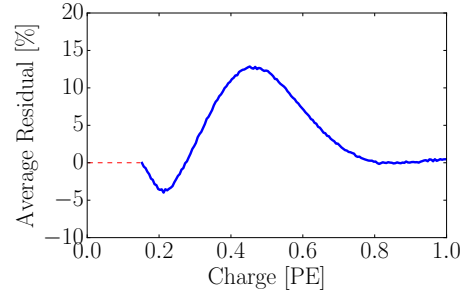


Figure 4. The extracted residual in blue, comparing the result of the convolutional fit to the data, averaged over all DOMs. The dashed red line indicates the region where we do not have sufficient data and therefore set the residual to 0% (i.e. no correction will be applied in this region).

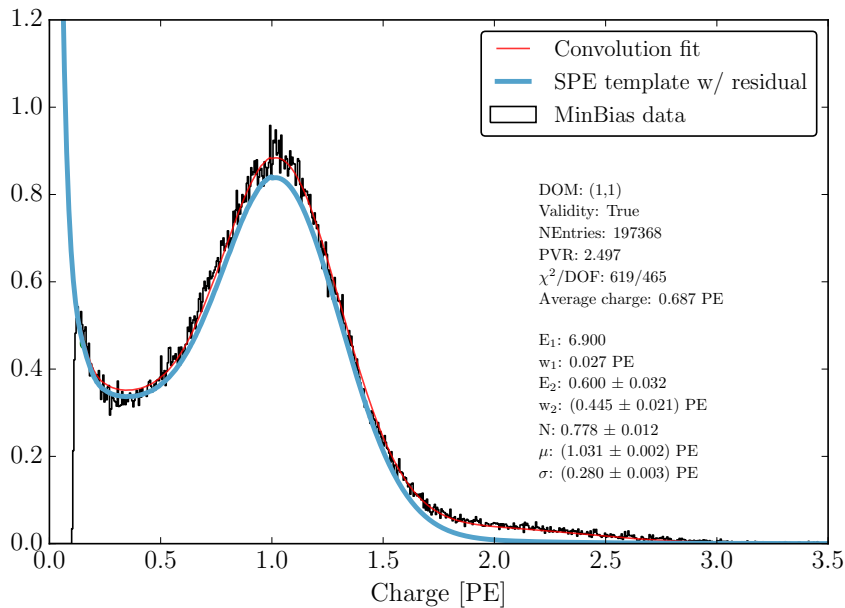


Figure 5. An example fit for DOM(1,1) using the MinBias dataset (black histogram) including data from seasons IC86.2011 to IC86.2016. The result of the convolution fit, which includes the 2 PE contribution, is shown as a solid red line and the extracted SPE charge template from the fit is shown in blue. For both the convolution fit and the SPE charge template, the curves include the correction from the average residual shown in Fig. 4.

508 E_2 component and $4.77 \pm 0.03\%$ smaller Gaussian amplitude. Consequently, the average HQE
509 peak-to-valley ratio is measured to be 2.322 ± 0.013 , corresponding to $12.12 \pm 0.06\%$ lower than
510 the average Standard QE DOMs. Also, interestingly, the average charge of the average HQE DOM
511 was found to be $3.34 \pm 0.01\%$ lower than that of the Standard QE DOMs. The average charge is
512 calculated by integrating over the full SPE charge template including the residual correction. The
513 values shown in Fig. 6 (right) are found to be below 1 PE due to the low-PE contribution from Exp_1
514 and Exp_2 , whose physical description can be found in Sec. 1.1.

515 IceCube compensates for the change in the mean measured charge in simulation, by increasing
516 the HQE DOM efficiency by the equivalent amount. This ensures that the total amount of charge
517 collected by the HQE DOMs remains the same prior to, and after, inserting the SPE charge templates
518 into simulation.

519 Similarly, using only the subset of Standard QE DOMs, the SPE charge templates compar-
520 ing the method of AC coupling were found to have measurably different shapes. The average
521 Gaussian amplitude and width for the DOMs instrumented with the old toroids were found to be
522 $8.31 \pm 0.01\%$ and $-6.80 \pm 0.03\%$, respectively. With these differences, we find a peak-to-valley ratio
523 of 2.643 ± 0.008 for the new toroid DOMs and 3.012 ± 0.012 for the old toroid DOMs. The average
524 Gaussian mean of the fit for the DOMs with the old toroids was also found to be $1.6 \pm 0.1\%$ lower
525 than those with the new toroids. This corresponds proportionally to a change in the expected gain.
526 The average charge, however, between these two hardware configurations remains very similar

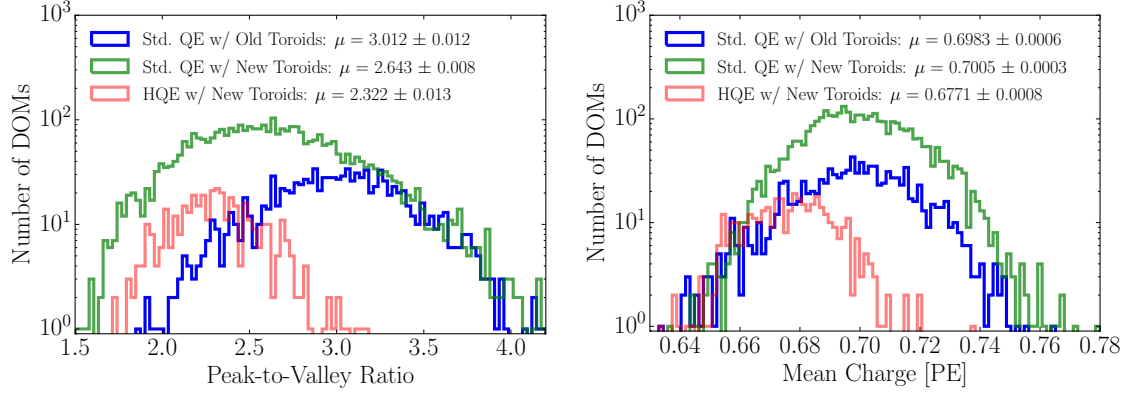


Figure 6. Comparison between the R7081-02MOD HQE DOMs and standard R7081-02 DOMs. Left: The peak-to-valley ratio for the two subsets of quantum efficiencies. Right: The average charge of the individual DOM SPE charge templates.

527 $(-0.346 \pm 0.001\%)$.

528 Although the DOMs instrumented with the old toroids were deployed into the ice earlier
 529 than those with the new toroids, the differences above are still noted when examining individual
 530 deployment years; therefore, the shape differences are not attributed to the change in the DOM
 531 behavior over time. However, the DOMs with the old toroids were the first PMTs to be manufactured
 532 by Hamamatsu. A gradual change of the fit parameters was observed when ordering the PMTs
 533 according to their PMT serial number (i.e. their manufacturing order). Fig. 7 shows the change in
 534 the measured peak-to-valley ratio as a function of PMT serial number for the standard QE DOMs
 535 (blue) and HQE PMTs (red). Here, each data point represents a single PMT and the blue (red)
 536 indicate a PMT instrumented with the new (old) toroid. This is compelling evidence that the
 537 observed differences between the new and old toroids is due to a change in the PMT production
 538 procedure rather than version of AC coupling.

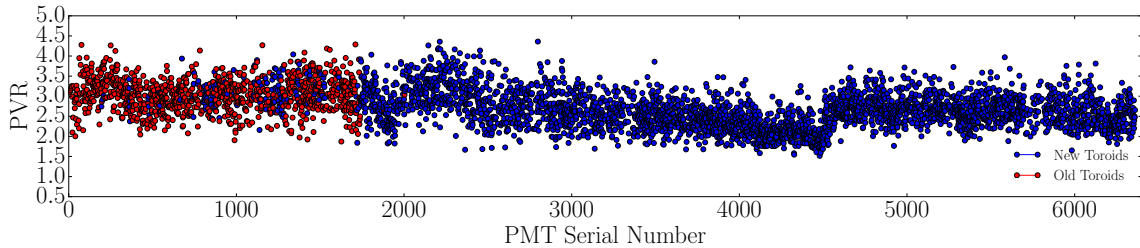


Figure 7. The measured peak-to-valley ratio for the standard QE PMTs ordered by PMT serial number. The red data points indicate a PMT instrumented with an old toroid, whereas new toroids are indicated by the blue data points.

539 Fig. 8 illustrates the average shape differences in the extracted SPE charge templates between the
 540 HQE DOM with the new toroids (solid white line), Standard QE with the new toroids (dotted white
 541 line), Standard QE with the old toroids (dashed white line), compared to the spread in the measured

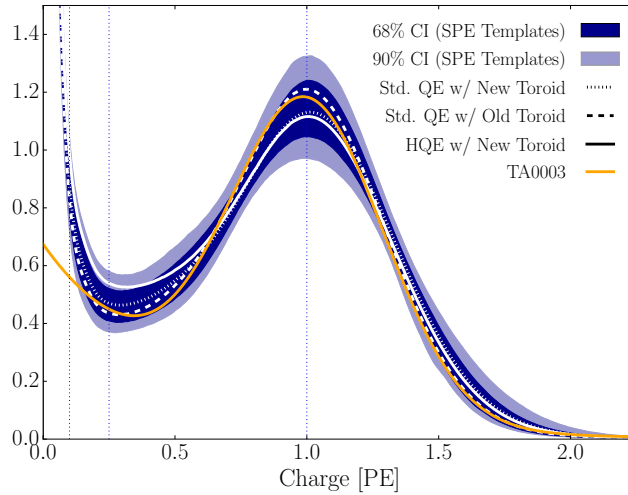


Figure 8. The inner (outer) dark blue region shows the 68% (90%) confidence interval defined by the measured spread in the extracted SPE charge templates of all DOMs in the detector. Superimposed are the average SPE charge templates for the variety of hardware configurations shown in white. The TA0003 distribution, for comparison, is shown in orange. All curves have been normalized such that the area above 0.25 PE is the same.

542 SPE charge templates for all DOMs in the detector (dark blue contours). The figure also shows
 543 how the previous default SPE charge distribution, the TA0003 distribution, compares to this recent
 544 measurement. All curves in this figure have been normalized such that the area above 0.25 PE is the
 545 same. The observable shape differences from the TA0003 are attributed to a better understanding
 546 of the low-charge region, the difference in functional form (described in Section 1.1), and the fact
 547 that the SPE charge templates were generated using a realistic photocathode illumination.

548 3.2 Fitting parameters variation over time

549 The SPE charge templates were extracted for each IceCube season independently to investigate the
 550 time dependence of the fit parameters. For every DOM in the detector, the change over time of each
 551 fit parameter (excluding Exp_1) was calculated. Fig. 9 shows the change in a given fit parameter,
 552 relative to the mean value, per year. The measured distribution was found to be consistent with
 553 statistically scrambling the yearly measurements. The average of each fit parameters are found to
 554 deviate less than 0.1%, which is in agreement with the stability checks performed in Ref. [9]. This
 555 observation holds for the individual subset of DOMs with different hardware configurations as well.

556 3.3 Quantifying observable changes when modifying the PMT charge distributions

557 Changing the assumed gain response in simulation has different implications depending on the
 558 typical illumination level present in different analyses. These differences are outlined in the
 559 following discussion.

560 The PMT response is described by a combination of a "bare" efficiency, η_0 , and a normalized
 561 charge response function, $f(q)$. The bare efficiency represents the fraction of arriving photons

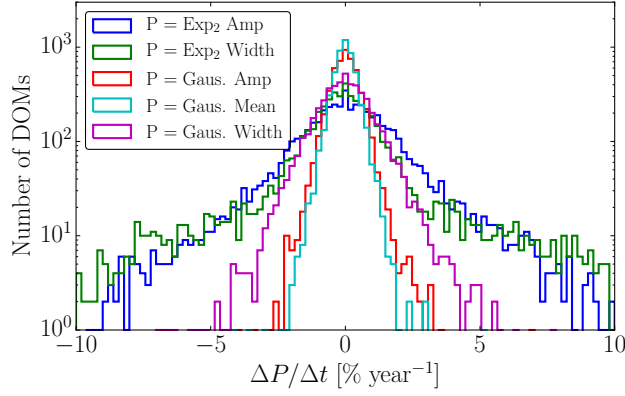


Figure 9. The change in the individual DOM fitted parameters over time, represented as percentage deviation from the mean fit parameter value.

562 that result in any nonzero charge response, including those below the discriminator threshold. The
 563 normalization condition is:

$$\int_0^{\infty} f(q) dq = 1. \quad (3.1)$$

564 Generally, $f(q)$ and η_0 have to be adjusted together to maintain agreement with a quantity known
 565 from lab or in-ice measurements, such as the predicted number of pulses above threshold for a dim
 566 source.

567 **Dim source measurements** Where light levels are low enough, the low occupancy ensures that
 568 sub-discriminator pulses do not contribute to any observed charge as they do not satisfy the trigger
 569 threshold. Given some independent way of knowing the number of arriving photons, a lab or in-ice
 570 measurement determines the trigger fraction above threshold $\eta_{0.25}$ and/or the average charge over
 571 threshold $Q_{0.25}$, either of which can be used to constrain the model as follows:

$$\eta_{0.25} = \eta_0 \int_{0.25q_{pk}}^{\infty} f(q) dq \quad (3.2)$$

$$Q_{0.25} = \eta_0 \int_{0.25q_{pk}}^{\infty} q f(q) dq \quad (3.3)$$

572 Here, the discriminator threshold is assumed to be 0.25 times the peak position q_{pk} . It is also
 573 useful to multiply observed charges by q_{pk} , since we set each PMT gain by such a reference, and
 574 then a measurement constraint would be stated in terms of $Q_{0.25}/q_{pk}$.

575 **Semi-bright source measurements** For semi-bright sources, pulses that arrive after the readout
 576 time window is opened are not subject to the the discriminator threshold. WaveDeform introduces
 577 a software termination condition at ~ 0.13 PE (described at the end of Section 2.1). The average
 578 charge of an individual pulse that arrives within the time window is:

$$Q_{0.10} = \eta_0 \int_{0.10q_{pk}}^{\infty} q f(q) dq \quad (3.4)$$

579 **Bright source measurements** For light levels that are large, the trigger is satisfied regardless
 580 of the response to individual photons, and the total charge per arriving photon therefore includes
 581 contributions below both the discriminator and the WaveDeform thresholds:

$$Q_0 = \eta_0 \int_0^{\infty} qf(q)dq \quad (3.5)$$

582 As such, the total charge is directly proportional to the average charge of the SPE charge
 583 template.

584 3.3.1 Model comparison

585 A natural question to ask is whether or not a change in $f(q)$ would cause observable changes in the
 586 bright-to-dim ratios. That is, when we change the SPE charge distribution in simulation, should
 587 we expect the charge collected by bright events compared to dim events to change? When the
 588 charge distribution model is changed in a way that preserves agreement with the measured $\eta_{0.25}$ or
 589 $Q_{0.25}/q_{pk}$, i.e. η_0 is adjusted properly for changes in $f(q)$, the physical effect can be summarized
 590 by the change in the bright-to-dim ratios $Q_0/Q_{0.25}$, and $Q_0/Q_{0.10}$. Conveniently, these ratios depend
 591 only on the shape of $f(q)$. Table 2 compares these ratios in terms of the TA0003 charge distribution
 592 and the SPE charge templates described here. It is shown that there are sub-percent level differences
 593 in the physically-observable bright-to-dim ratios. The largest difference in the shape between the
 594 SPE charge templates and the TA0003 distribution is in the low-charge region, particularly below
 595 ~ 0.10 PE. Charge from this region can only inflate bright events. That is, these pulses are small to
 596 trigger the discriminator or be reconstructed by WaveDeform, however they can reside on top of
 597 other pulses, inflating them. Since these pulses by definition contain little charge, they do not tend
 598 to inflate the measured charge by a noticeable amount, as shown by the $Q_0/Q_{0.25}$ measurements in
 599 Table 2.

Model	Detector	$Q_0/Q_{0.25}$	$Q_0/Q_{0.10}$	$\eta_{0.25}/Q_{0.25}$
TA0003	All DOMs	1.017	1.0031	1.05
SPE charge templates	HQE + New Toroids	1.021 ± 0.002	1.0041 ± 0.0004	1.05 ± 0.02
	Std. QE + New Toroids	1.018 ± 0.002	1.0035 ± 0.0005	1.03 ± 0.02
	Std. QE + Old Toroids	1.017 ± 0.002	1.0033 ± 0.0005	1.05 ± 0.02

Table 2. The distribution in bright-to-dim ratios for the previous charge distribution (TA0003) and the individual DOM SPE charge templates for the IceCube and DeepCore detectors.

600 3.4 SPE charge templates for calibration

601 The gain setting on each PMT is calibrated prior to the beginning of each season such that the
 602 Gaussian mean of the charge distribution corresponds to a gain of 10^7 , or equivalently 1 PE.
 603 This gain calibration method, run directly on the DOMs, uses waveform integration for charge
 604 determination instead of WaveDeform unfolding, resulting in a small systematic shift in gain. This
 605 systematic shift was determined for every PMT. The mean shift obtained over all DOM was found
 606 to be $2.00 \pm 0.03\%$ with a standard deviation of 3.54%, corresponding to an overestimation of the
 607 measured charge in the detector.

608 The correction to the systematic shift in the measured charge can be implemented retroactively
609 by dividing the reported charge from WaveDeform by the corresponding offset for a given DOM.
610 Alternatively, we can account for this by simply inserting SPE charge templates, measured in this
611 analysis, into simulation such that the corresponding systematic shift is also modelled in simulation.
612 This will be performed in the following subsection.

613 3.5 SPE charge templates in simulation

614 To model the IceCube instrument, we must implement the PMT response in simulation. The
615 IceCube MC simulation chain assigns a charge to every photoelectron generated at the surface of
616 the photocathode. The charge is determined by sampling from a normalized charge distribution
617 probability density function (PDF). A comparison to data between describing the charge distribution
618 PDF using the SPE charge templates and the TA0003 distribution follows.

619 Two simulation sets consisting of the same events were processed through the IceCube Monte
620 Carlo simulation chain to the final analysis level of an update to the IC86.2011 sterile neutrino analy-
621 sis [24]. Here, the events that pass the cuts are >99.9% upward-going (a trajectory oriented upwards
622 relative to the horizon) secondary muons produced by charged current muon neutrino/antineutrino
623 interactions. The muon reconstructed energy range of this event selection is between approximately
624 500 GeV and 10 TeV.

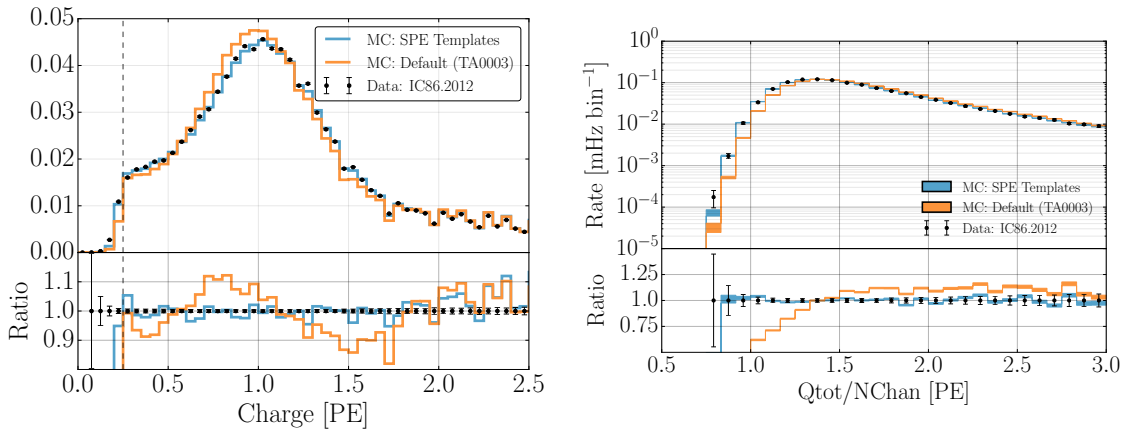


Figure 10. A comparison between the SPE charge templates (blue) and the TA0003 (orange) model for describing the SPE charge distribution in Monte Carlo. The simulation is compared to the 2012 IceCube season. The data is shown in black. Left: The total measured charge per DOM, per event at analysis level. Right: The distribution of the total measured charge of an event divided by the number of DOMs that participated in the event.

625 Fig. 10 (left) shows the distribution of the total measured charge during each event per DOM
626 (data points). The simulation set using the TA0003 charge distribution is shown in orange, and that
627 using the SPE charge templates is shown in blue. The data is shown for the full IC86.2012 season
628 but is statistically equivalent to any of the other seasons. Fig. 10 (right) shows the distribution of
629 the total measured charge of an event divided by the number of channels (NChan), or DOMs, that
630 participated in the event. Both plots in Fig. 10 have been normalized such that the area under the
631 histograms is the same.

632 The SPE charge templates clearly improve the overall MC description of these two variables.
633 This update may be useful for analyses that rely on low-occupancy events (low-energy or dim
634 events) in which average charge per channels is below 1.5 PE, and will be investigated further
635 within IceCube.

636 **4 Conclusion**

637 This article outlines the procedure used to extract the SPE charge templates for all in-ice DOMs in the
638 IceCube detector using in-situ data from IC86.2011 to IC86.2016. The result of this measurement
639 was shown to be useful for improving the overall data/MC agreement as well as calibration of the
640 individual PMTs. It also prompted a comparison between the shape of the SPE charge templates
641 for a variety of hardware configurations and time dependent correlations.

642 The subset of HQE DOMs were found to have a smaller peak-to-valley ratio relative to the
643 Standard QE DOMs, as well as an overall $3.34 \pm 0.01\%$ lower average charge. It was also found
644 that the DOMs instrumented with the old toroids used for AC coupling (the first PMTs to be
645 manufactured by Hamamatsu) had narrower and larger Gaussian component corresponding resulting
646 in an increased peak-to-valley ratio of $14.0 \pm 0.6\%$. This was found to be likely due to a change
647 in the manufacturing over time rather than the actual AC coupling method. No significant time
648 dependence in any of the fitted parameters associated with the SPE charge templates over the
649 investigated seasons was observed. A reassessment of the PMT gain settings found a systematic
650 bias of $2.00 \pm 0.03\%$ with a standard deviation of 3.54% .

651 The SPE charge templates were inserted into the MC simulation and the results were compared
652 to the default TA0003 distribution. A significant improvement in the description of the variables
653 total charge per DOM and total charge over the number of channels was shown. Analyses which rely
654 on low-light occupancy measurements, may benefit from this update. As shown in the bright-to-dim
655 ratios, the average average charge for various light levels will not be affected by this update.

656 **Acknowledgments**

657 We acknowledge the support from the following agencies:

658 USA – U.S. National Science Foundation-Office of Polar Programs, U.S. National Science
659 Foundation-Physics Division, Wisconsin Alumni Research Foundation, Center for High Throughput
660 Computing (CHTC) at the University of Wisconsin-Madison, Open Science Grid (OSG), Extreme
661 Science and Engineering Discovery Environment (XSEDE), U.S. Department of Energy-National
662 Energy Research Scientific Computing Center, Particle astrophysics research computing center at
663 the University of Maryland, Institute for Cyber-Enabled Research at Michigan State University, and
664 Astroparticle physics computational facility at Marquette University; Belgium – Funds for Scien-
665 tific Research (FRS-FNRS and FWO), FWO Odysseus and Big Science programmes, and Belgian
666 Federal Science Policy Office (Belspo); Germany – Bundesministerium für Bildung und Forschung
667 (BMBF), Deutsche Forschungsgemeinschaft (DFG), Helmholtz Alliance for Astroparticle Physics
668 (HAP), Initiative and Networking Fund of the Helmholtz Association, Deutsches Elektronen Syn-
669 chrotron (DESY), and High Performance Computing cluster of the RWTH Aachen; Sweden –
670 Swedish Research Council, Swedish Polar Research Secretariat, Swedish National Infrastructure
671 for Computing (SNIC), and Knut and Alice Wallenberg Foundation; Australia – Australian Re-
672 search Council; Canada – Natural Sciences and Engineering Research Council of Canada, Calcul
673 Québec, Compute Ontario, Canada Foundation for Innovation, WestGrid, and Compute Canada;
674 Denmark – Villum Fonden, Danish National Research Foundation (DNRF), Carlsberg Foundation;
675 New Zealand – Marsden Fund; Japan – Japan Society for Promotion of Science (JSPS) and Institute
676 for Global Prominent Research (IGPR) of Chiba University; Korea – National Research Foundation
677 of Korea (NRF); Switzerland – Swiss National Science Foundation (SNSF); United Kingdom –
678 Department of Physics, University of Oxford.

679 **References**

- 680 [1] J. Ahrens et al., *IceCube preliminary design document*, URL:
681 <https://icecube.wisc.edu/icecube/static/reports/IceCubeDesignDoc.pdf> (2001) .
- 682 [2] A. Achterberg et al., *First year performance of the IceCube neutrino telescope*, *Astroparticle Physics*
683 **26** (2006) 155–173, [[arXiv:astro-ph/0604450v2](https://arxiv.org/abs/astro-ph/0604450v2)].
- 684 [3] M. G. Aartsen et al., *Evidence for high-energy extraterrestrial neutrinos at the IceCube detector*,
685 *Science* **342** (2013) 1242856, [[arXiv:1311.5238v2](https://arxiv.org/abs/1311.5238v2)].
- 686 [4] R. Abbasi et al., *The design and performance of IceCube DeepCore*, *Astroparticle Physics* **35** (2012)
687 615–624, [[arXiv:1109.6096v1](https://arxiv.org/abs/1109.6096v1)].
- 688 [5] R. Abbasi et al., *The IceCube data acquisition system: Signal capture, digitization, and timestamping*,
689 *NIM-A* **601** (2009) 294–316, [[arXiv:0810.4930v2](https://arxiv.org/abs/0810.4930v2)].
- 690 [6] M. Aartsen et al., *Measurement of South Pole ice transparency with the IceCube LED calibration*
691 *system*, *NIM-A* **711** (2013) 73–89, [[arXiv:1301.5361v1](https://arxiv.org/abs/1301.5361v1)].
- 692 [7] R. Abbasi et al., *IceTop: The surface component of IceCube*, *NIM-A* **700** (2013) 188–220.
- 693 [8] R. Abbasi et al., *Calibration and characterization of the IceCube photomultiplier tube*, *NIM-A* **618**
694 (2010) 139–152, [[arXiv:1002.2442v1](https://arxiv.org/abs/1002.2442v1)].
- 695 [9] M. G. Aartsen et al., *The IceCube Neutrino Observatory: Instrumentation and Online Systems*, *JINST*
696 **12** (2017) 1748–0221, [[arXiv:1612.05093v2](https://arxiv.org/abs/1612.05093v2)].
- 697 [10] M. Aartsen et al., *Energy reconstruction methods in the IceCube Neutrino Telescope*, *JINST* **9** (2014)
698 1748–0221, [[arXiv:1311.4767v3](https://arxiv.org/abs/1311.4767v3)].
- 699 [11] R. Stokstad, *Design and performance of the IceCube electronics*,
700 URL: <https://cds.cern.ch/record/920022/files/p20.pdf> (2005) .
- 701 [12] Hamamatsu, *Resources: Basics and Applications*,
702 URL: https://www.hamamatsu.com/resources/pdf/etd/PMT_handbook_v3aE.pdf (2018) .
- 703 [13] Hamamatsu, *Handbook Resources, Chapter 4*, URL: https://www.hamamatsu.com/resources/pdf/etd/PMT_handbook_v3aE-Chapter4.pdf (2018) .
- 704 [14] J. Brack et al., *Characterization of the Hamamatsu R11780 12 in. photomultiplier tube*, *NIM-A* **712**
705 (2013) 162–173, [[arXiv:1210.2765v2](https://arxiv.org/abs/1210.2765v2)].
- 706 [15] E. Calvo et al., *Characterization of large-area photomultipliers under low magnetic fields: Design*
707 *and performance of the magnetic shielding for the Double Chooz neutrino experiment*, *NIM-A* **621**
708 (2010) 222–230, [[arXiv:0905.3246v1](https://arxiv.org/abs/0905.3246v1)].
- 709 [16] F. Kaether and C. Langbrandtner, *Transit time and charge correlations of single photoelectron events*
710 *in R7081 photomultiplier tubes*, *JINST* **7** (2012) P09002, [[arXiv:1207.0378v2](https://arxiv.org/abs/1207.0378v2)].
- 711 [17] B. Lubsandorzhev, P. Pokhil, R. Vasiljev and A. Wright, *Studies of prepulses and late pulses in the 8"*
712 *electron tubes series of photomultipliers*, *NIM-A* **442** (2000) 452–458.
- 713 [18] K. Ma et al., *Time and amplitude of afterpulse measured with a large size photomultiplier tube*,
714 *NIM-A* **629** (2011) 93–100, [[arXiv:0911.5336v1](https://arxiv.org/abs/0911.5336v1)].
- 715 [19] S. Torre, T. Antonioli and P. Benetti, *Study of afterpulse effects in photomultipliers*, *Review of*
716 *Scientific Instruments* **54** (1983) 1777–1780.
- 717 [20] Hamamatsu, *Photomultiplier tubes: Construction and Operating Characteristics*,
718 URL: https://www.hamamatsu.com/resources/pdf/etd/PMT_TPMZ0002E.pdf (2016) .
- 719

- 720 [21] M. Aartsen et al., *Characterization of the atmospheric muon flux in IceCube*, *Astroparticle Physics* **78**
721 (2016) 1–27, [[arXiv:1506.07981v2](#)].
- 722 [22] M. Aartsen et al., *Search for steady point-like sources in the astrophysical muon neutrino flux with 8*
723 *years of IceCube data*, *The European Physical Journal C* **79** (2019) 234, [[arXiv:1811.07979v2](#)].
- 724 [23] R. Dossi, A. Ianni, G. Ranucci and O. J. Smirnov, *Methods for precise photoelectron counting with*
725 *photomultipliers*, *NIM-A* **451** (2000) 623–637.
- 726 [24] M. Aartsen et al., *Searches for sterile neutrinos with the IceCube detector*, *Physical Review Letters*
727 **117** (2016) 071801, [[arXiv:1605.01990v2](#)].